Materials Advances

ROYAL SOCIETY OF CHEMISTRY

PAPER

View Article Online
View Journal

Cite this: DOI: 10.1039/d5ma01208b

$CsPbBr_3$ crystal growth *via* antisolvent vapor assisted method and their photoelectric properties

Maksym Pecherkin, *[a] Vasyl Mykhailovych, *[b] Matthias Gutmann,[c] Gheorghe Lucian Păşcuţ,[d] Petro Fochuk,*[a] Mariia Mykhailovych,[e] Aurelian Rotaru,[e] Yuriy Khalavka [a] and Andriy Dmytruk [f]

Received 20th October 2025,
Accepted 30th March 2026

DOI: 10.1039/d5ma01208b

rsc.li/materials-advances

Inorganic halide perovskites, particularly $CsPbBr_3$, have emerged in recent years as promising materials for optoelectronic applications due to their easily tunable bandgap, high charge carrier mobility, and radiation sensing capabilities. This study describes an efficient and straightforward method for growing high-quality $CsPbBr_3$ single crystals using the antisolvent vapor-assisted method, using nitromethane as the antisolvent within a temperature range of 25–45 °C. The resulting crystal has an optical bandgap of about 2.28 eV. X-ray structural analysis confirms the orthorhombic phase. Optical and photoelectrical measurements reveal a clear photocurrent response under UV irradiation at 365 nm, marked by a evident increase in photocurrent density. In addition, the charge carrier mobility–lifetime product extracted from charge collection efficiency analysis reaches $\sim 0.8 \times 10^{-3}$ cm^2 V^{-1}, indicating efficient charge transport. Under visible-light illumination at 530 nm, the crystals demonstrate a responsivity of 6.24×10^{-3} A W^{-1} and a specific detectivity of $\sim 1.3 \times 10^{10}$ Jones. Surface morphology assessed by scanning electron microscopy (SEM) confirms the high surface quality of the crystals. These findings highlight the potential of this modified growth method for producing $CsPbBr_3$ single crystals suitable for next-generation photodetectors and other optoelectronic devices.

1. Introduction

The development of high-performance γ-ray and X-ray detectors remains a critical challenge for modern technologies in astrophysics, nuclear energy, radiation safety, and medical diagnostics.[1–3] Stringent requirements for high energy resolution, stable operation at room temperature, and scalable manufacturing significantly restrict the range of suitable semiconductor materials. Although cadmium zinc telluride (CZT)-based detectors can achieve energy resolutions of approximately 1–2% at 662 keV, their broader implementation is limited by high material cost, difficulties in growing large-volume single crystals, and substantial technological complexity during fabrication.[2,3]

In this context, lead halide perovskites have emerged as promising alternatives to conventional semiconductor detector materials. These compounds combine a high absorption coefficient, a tunable bandgap in the range of ~1.4–2.3 eV, low concentrations of deep-level defects, and long charge-carrier diffusion lengths.[4–7] In particular, solution-grown perovskite single crystals have been reported to exhibit electron and hole diffusion lengths exceeding 175 μm, which are comparable to or even surpass those of many established detector materials.[4,6] In addition, theoretical studies have confirmed the high defect tolerance of inorganic perovskites, including $CsPbBr_3$, enabling efficient charge transport even in the presence of structural imperfections.[7]

Among lead halide perovskites, the fully inorganic compound $CsPbBr_3$ occupies a distinctive position due to its enhanced thermal and phase stability compared to hybrid analogues.[8–11] $CsPbBr_3$ single crystals have been shown to deliver γ-ray spectroscopic energy resolutions of approximately 1.9–2.3% at 662 keV under room-temperature operation, approaching the performance of state-of-the-art CZT detectors.[8,11] Furthermore, the mobility–lifetime product ($\mu\tau$) in $CsPbBr_3$ has been reported to

[a] Department of Chemistry and Food Expertise, Yuriy Fedkovych Chernivtsi National University, 2, Kotsjubynskyi St., 58012 Chernivtsi, Ukraine. E-mail: pecherkin.maksym@chnu.edu.ua, p.fochuk@chnu.edu.ua
[b] Technology Transfer Center in Industry 4.0 and Smart Destinations & Department of Electrical Engineering and Computer Science, Stefan Cel Mare University of Suceava, 720229 Suceava, Romania. E-mail: vasyl.mykhailovych@usm.ro
[c] Harwell Science and Innovation Campus, Rutherford Appleton Laboratory, ISIS Facility, Chilton Didcot, Oxfordshire OX11 0QX, UK
[d] Faculty of Forestry, Stefan Cel Mare University of Suceava, Suceava 720229, Romania
[e] Department of Electrical Engineering and Computer Science & Research Center Mansid, Stefan Cel Mare University of Suceava, 720229 Suceava, Romania
[f] Institute of Physics of National Academy of Sciences of Ukraine, Kyiv, Ukraine

reach values on the order of 10^{-3}–10^{-2} cm^2 V^{-1}, which is a key requirement for efficient detection of ionizing radiation.[9,12,13]

Traditionally, detector-grade $CsPbBr_3$ single crystals have been obtained *via* melt-growth techniques, most notably the vertical Bridgman method, which enables the production of large crystals with high chemical purity and favorable spectroscopic characteristics. For instance, He *et al.*[11] demonstrated that centimeter-scale $CsPbBr_3$ single crystals grown from the melt exhibit total impurity concentrations below 10 ppm (considering 69 elements) and achieve energy resolutions of 3.9% at 122 keV and 3.8% at 662 keV; the efficient detector response was attributed to hole transport with $(\mu\tau)_h \approx 1.34 \times 10^{-3}$ cm^2 V^{-1} and carrier lifetimes exceeding 25 μs. Despite these advantages, melt-growth approaches are technologically demanding and energy intensive: $CsPbBr_3$ melts at temperatures of approximately 567–568 °C, while the melting and crystallization processes exhibit complex kinetics, a two-stage mechanism, and pronounced sensitivity to heating and cooling rates (≈0.1–10 °C min^{-1}). These factors significantly complicate reproducibility and large-scale implementation. Thermal studies have further revealed high activation energies for melting and crystallization (exceeding 10^3 kJ mol^{-1}), highlighting the need for precise temperature control and sophisticated equipment in melt-growth processes.[10]

Nevertheless, it has been shown that even when melt-growth is scaled to large dimensions, with crystal diameters reaching ~65 mm, $CsPbBr_3$ can still exhibit excellent detector performance. In particular, Toufanian *et al.*[14] reported energy resolutions of approximately 2% at 662 keV, photopeak-to-Compton ratios up to 14.3, and $\mu\tau$ values as high as $\sim 1.7 \times 10^{-2}$ cm^2 V^{-1}. At the same time, their results revealed that polarization effects and signal stability strongly depend on crystal quality and the orientation of the applied electric field relative to the crystallographic axes. These observations underscore both the high potential of $CsPbBr_3$ and the sensitivity of melt-grown detectors to subtle variations in growth and processing conditions.

In parallel with the development of melt-growth techniques, substantial progress has been achieved in the solution growth of $CsPbBr_3$ single crystals under mild thermodynamic conditions. Dirin *et al.*[9] demonstrated that solution-grown $CsPbBr_3$ single crystals exhibit efficient charge transport with typical $\mu\tau$ values on the order of 10^{-3} cm^2 V^{-1}, which are sufficient for detector applications. Further advances in solution-based methods, including inverse temperature crystallization (ITC), enabled the rapid growth of high-quality bulk perovskite single crystals within minutes at temperatures below 100–120 °C, accompanied by reduced trap densities and high structural uniformity.[15] For inorganic perovskites such as $CsPbBr_3$, phase-selective low-temperature growth strategies have provided precise control over crystal phase and carrier concentration, leading to extremely low minority carrier densities (~10^8 cm^{-3}) and enabling self-powered photodetector operation without external bias.[16] At the level of photoelectric response, such single crystals exhibit pronounced photoconductivity, with photocurrents increasing by 2–3 orders of magnitude under illumination, typical current values of $\sim 10^{-8}$–10^{-7} A, and stable ON/OFF ratios reaching 10^4–10^5. These characteristics are consistent with reported responsivities of ~0.02–0.03 A W^{-1} and detectivities up to ~10^{11} Jones in $CsPbBr_3$ single-crystal photodetectors.[12,15] Moreover, Rakita *et al.* demonstrated that low-temperature solution-based growth approaches for $CsPbBr_3$, including slow saturation of the precursor solution with antisolvent vapor (VSA) and the exploitation of retrograde solubility upon heating, enable the formation of millimeter-scale single crystals with a 100% perovskite phase yield and a high degree of phase purity; the resulting crystals exhibit carrier lifetimes of approximately 30 ns and low Urbach energies (~19 meV), indicative of favorable structural and optical characteristics.[17] Collectively, these studies demonstrate that solution-based growth methods can deliver detector-relevant transport and photoelectric properties while substantially reducing technological complexity compared to melt-growth approaches.

In view of these considerations, the objective of the present work is to further advance a solution-based strategy for the synthesis of $CsPbBr_3$ single crystals by controlling crystallization kinetics using an antisolvent vapor-assisted (AVS) approach. Here, we report a modified and technologically simplified AVS method that enables the direct growth of $CsPbBr_3$ single crystals with a cuboid morphology and characteristic dimensions of approximately $5 \times 5 \times 2.5$ mm^3. The resulting crystals exhibit a combination of electrical and photoelectric properties that indicates their potential for further optoelectronic and radiation-detector applications, while relying on readily available precursors of basic purity.

2. Experimental section

2.1 Materials

$PbBr_2$ (≥ 98%), CsBr (≥ 99.9%), dimethyl sulfoxide (DMSO, ≥99.9%) were purchased from Sigma-Aldrich. Choline bromide (CB, ≥98%) was purchased from TCI America, nitromethane (CH_3NO_2, ≥99%), and ethyl acetate (EA, 99.5%) where purchased from Thermo Fisher Scientific.

2.2 Preparation of precursor solution

A standard $CsPbBr_3$ precursor solution was obtained by dissolving CsBr (0.6 mmol) and $PbBr_2$ (1.2 mmol) in a molar ratio of 1 : 2 to improve component solubility,[9] in 3 ml of DMSO. Additionally, 0.1 mmol of choline bromide was added to the precursor solution. The precursor solutions were gradually heated to 70 °C to accelerate dissolution with constant stirring until fully dissolved. After complete dissolution, heating and stirring were stopped. The solutions were then filtered using a PTFE filter with a pore size of 0.22 μm.

2.3 Growth of $CsPbBr_3$ single crystal

The filtered precursor solution was transferred into a clean crystallization vial, which was covered with aluminium foil. A small hole (~0.5 mm) was pierced beforehand.

This vial containing the precursor solution was placed into a large flat-bottomed beaker containing CH_3NO_2. The outer

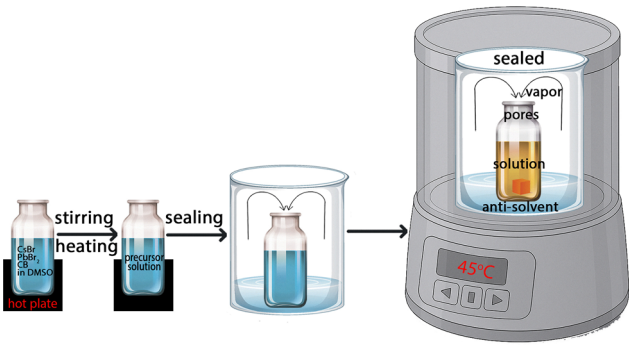

Fig. 1 Schematics step-by-step illustration of the $CsPbBr_3$ synthesis and single crystals growth.

beaker was sealed using several layers (5–10) of polyethylene film to minimize vapor pressure loss of the antisolvent. The beaker was then placed into a dry-air thermostat and heated to 45 °C. The crystallization process took about 120 hours. After 120 hours, the container was removed from the thermostat, and it consistently yielded one large single crystal of approximately 5 × 5 × 2.6 mm in size, along with a small number of smaller crystals. The grown crystal was extracted from the solution and carefully washed with ethyl acetate to prepare it for further surface treatment (Fig. 1).

2.4 Device fabrication

The fabrication of the device to test the photocurrent of the $CsPbBr_3$ single crystal sample involved several stages, including step-by-step surface preparation, forming well-defined edges, and maintaining uniform geometric parameters of the crystals. To achieve this, the sample was pre-polished using abrasive powders of varying grain sizes to obtain a uniform and optically flat crystal surface. Mostly, powders with grain sizes of 1–0.3 μm were used. The surface treatment was conducted on an abrasive surface with 5000 grit. After each polishing step, the crystal was carefully washed with ethyl acetate. After the final polishing stage, the sample had well-defined edges and an optically smooth surface suitable for electrode deposition. Gold was used as the electrode material because it provides a high-quality contact with the surface and reliable ohmic contacts. Gold contacts (Au) with a thickness of 150 nm were deposited on opposite faces of the crystal using a sputter coating method (Quorum Sputter Coater, Model Q150TES) through appropriate masks with a circular aperture of 3.2 mm in diameter.

2.5 Materials characterization of $CsPbBr_3$ crystals

The morphological and elemental analyses of crystal were performed using a Hitachi SU-70 field emission scanning electron microscope (FE-SEM) equipped with an Oxford Instrument EDX-detector. The phase formation and purity of the $CsPbBr_3$ crystal structure were examined by single crystal X-ray diffraction. Rigaku-Oxford Diffraction XTaLab Synergy S diffractometer equipped with a HyPix6000 area detector at room temperature using Mo wavelength (λ = 0.7093 Å for Kα1 radiation) has been used. Data reduction was done using CrysAlisPro. The structure was refined using the JANA2020 program[18] taking into account twin domains.

Photocurrent measurements were performed on single crystals of cesium lead bromide ($CsPbBr_3$). The samples were mounted in a two-electrode configuration with gold contacts deposited on opposite crystal surfaces. The electrodes were connected to a source-measure unit (Keithley 2400, USA), which provided a controlled bias voltage and recorded the photocurrent response.

For optical excitation, two types of lamps were employed: a fluorescent lamp Philips MASTER TL-D 18W/840 (room/day light) and a UV lamp Spectroline E-Series, 365 nm. All measurements were carried out at room temperature under ambient atmosphere. The UV lamp (Spectroline E-Series, 365 nm) was used with a normalized intensity of 5200 μW cm^{-2}. The UV-VIS, PL spectra were recorded using an OceanOptics USB2000 and Cary 60 UV-Vis spectrophotometer.

Time-resolved photoluminescence (TRPL) measurements were performed using a multi-pixel photon counter (MPPC, Hamamatsu S12572-050) positioned at the side exit of an Acton Research SP-2500i monochromator equipped with a 1200 grooves per mm diffraction grating blazed at 500 nm. Optical excitation was provided by 400 nm laser pulses with a duration of 150 fs and a repetition rate of 1 kHz, generated as the second harmonic of the fundamental emission of a Coherent Ti:Sa Legend-HE amplifier seeded by a Mira-900F oscillator. The instrument response function (IRF) was measured at 530 nm using the second harmonic of the emission from a Coherent OperA optical parametric amplifier. The MPPC signal, terminated with a 50 Ω load, was recorded using a RIGOL DS5202MA digital oscilloscope with 256-sample signal averaging. The acquired TRPL data were processed using specially developed software,[19] which enabled deconvolution of the measured signals using mono- or bi-exponential decay models. Impedance spectroscopy measurements for the independent assessment of the charge mobility product were performed using a CONCEPT 40 Broadband Dielectric Spectrometer (Novocontrol Technologies GmbH & Co. KG, Montabaur, Germany) equipped with an Alpha-A high performance frequency analyzer.

3. Results and discussion

Previous studies have shown that lead halide perovskites such as $MAPbX_3$ (X = Br^- and I^-) and $CsPbBr_3$ exhibit retrograde solubility in solvents like gamma-butyrolactone (GBL), *N*,*N*-dimethylformamide (DMF), and dimethyl sulfoxide (DMSO). Therefore, we employed the anti-solvent precipitation method, one of the most accessible and efficient approaches for growing high-quality $CsPbBr_3$ single crystals. This method is based on the gradual reduction of precursor solubility in the solution using an anti-solvent that saturates the solution with its vapours, leading to supersaturation and initiating crystallization. Common anti-solvents include methanol, acetonitrile, and water. In our case, CH_3NO_2 was chosen due to its physicochemical properties—particularly its density and boiling

point—which result in slower vapor diffusion and more uniform solution saturation. However, the effectiveness of crystallization in the AVS process is governed not only by diffusion kinetics, but also by the ability of the antisolvent to modify the solvation environment of ionic species in solution, especially haloplumbate complexes $[PbBr_x]^{(2-x)-}$. The diffusion of antisolvent vapors alters the effective dielectric permittivity of the medium and the stability of Pb–solvent coordination bonds, thereby shifting the equilibrium among different Pb–Br complex species and, consequently, influencing the nucleation and crystal growth kinetics. Nitromethane (CH_3NO_2), as a polar aprotic antisolvent with a relatively high dielectric constant ($\varepsilon \approx 36$), enables a more controlled decrease in precursor solubility and a "milder" solvation rearrangement without hydrolytic effects, which favors stable supersaturation and the growth of high-quality perovskite single crystals. In contrast, water, despite its much higher dielectric constant ($\varepsilon \approx 78$–80), is a protic medium and may induce hydrolytic/degradation processes and uncontrolled nucleation by strongly perturbing complexation equilibria, ultimately reducing the reproducibility of the growth process and the quality of the resulting crystals. Similar considerations also apply to more volatile antisolvents such as acetonitrile (CH_3CN) and methanol (CH_3OH), where faster vapor diffusion may further accelerate supersaturation and nucleation, making controlled crystal growth more challenging.

In the study by Feng *et al.*,[20] the effectiveness of using CB as an additive for growing $CsPbBr_3$ single crystals using the ITC method was demonstrated. Adding CB to the precursor solution altered the crystal morphology. The role of CB in modulating crystal growth is attributed to its selective interaction with Br-rich crystal facets. The positively charged quaternary ammonium group in the CB molecule can adsorb onto fast-growing planes, particularly the (002) facet, *via* electrostatic interactions, thereby blocking further attachment of Cs^+ or Pb^{2+} ions. This suppresses the growth rate along the [002] direction, promoting a transition from anisotropic, rod-like growth to isotropic cuboid morphology. The mechanism is further supported by a significant reduction in trap density and improved crystal symmetry, despite the absence of direct *in situ* observations. However, growing crystals using the ITC method is more time-consuming and complex, requiring seed preparation and precise, uniform heating of the mixture at a rate of 0.1–1 °C h^{-1}. To simplify the growth of bulk $CsPbBr_3$ crystals with well-defined edges, we adapted a more efficient and straightforward approach based on the anti-solvent precipitation method with the addition of CB to grow high-quality crystals. Furthermore, we simplified the anti-solvent method by eliminating the need for prior precursor solution titration. The modified method and optimized synthesis conditions allow the growth of cuboid-shaped single crystals with sizes around 5 × 5 × 2.6 mm or larger.

3.1 Room temperature single crystal diffraction

Diffraction patterns and illustration of twin lattice (2 domains) are depicted in Fig. S1. The presence of twinning is also reflected in the relatively higher R_{int} value of 0.1419 details of the refinement are listed in Table S1 (see in SI). The refined unit cell parameters are: a = 8.2289(2) Å, b = 8.2289(2) Å, and c = 11.7196(6) Å, resulting in a unit cell volume of 793.59 $Å^3$.

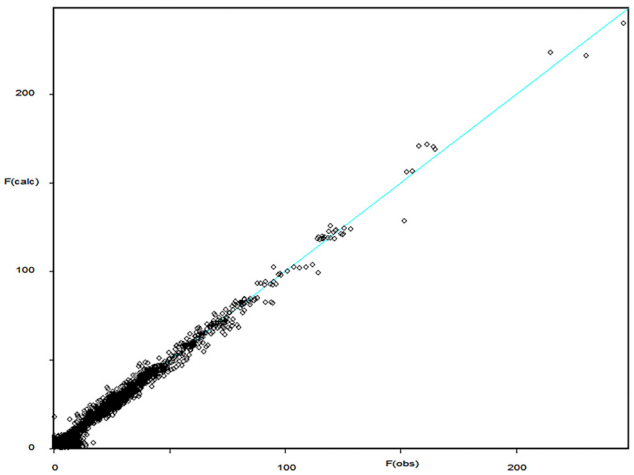

Fig. 2 Observed (*F*(obs)) *vs.* calculated (*F*(calc)) intensities from the single crystal refinement.

The experimental and calculated diffraction intensities of $CsPbBr_3$ single crystal synthesized by antisolvent vapor assisted method are shown in Fig. 2. All the experimental diffraction peaks matched the calculated ones, confirming that the crystal structure corresponds to an orthorhombic perovskite structure with *Pbnm* symmetry. Such symmetry was also obtained by authors[10,20–22] using ITC, additive assisted method and solution growth.

To further evaluate the crystalline quality, a rocking curve measurement was performed. Fig. 3 shows the rocking curve for the (0, −4, 0) reflection. The full width at half maximum is 0.273(5) degrees as determined from numerical fitting using a Gaussian. This relatively narrow FWHM value indicates that the obtained $CsPbBr_3$ crystal possesses good crystallinity.

3.2 Optical measurements

The optical properties of the obtained $CsPbBr_3$ sample were investigated, including absorption and photoluminescence (PL). Fig. 4a shows the absorption spectrum of the single crystal, where a distinct absorption shoulder can be seen in the 540–560 nm range, which is characteristic of $CsPbBr_3$ perovskite samples. From the absorption spectrum, the energy band gap was determined using the Tauc method, yielding a value of 2.28 eV, as shown in Fig. 4b.

The emission properties of this sample were also measured in the form of photoluminescence, with a peak at approximately 538 nm (Fig. 4c).

The optical properties of $CsPbBr_3$ single crystals were investigated at room temperature. Fig. S4 presents the transmission spectrum in the range of 300–950 nm. A sharp absorption edge is observed at around 530–550 nm, which is consistent with reported values for $CsPbBr_3$.[16,23,24] Above this edge, the crystals exhibit a relatively high average transmittance of ~58% in the 550–900 nm region, confirming their high optical quality and phase purity.

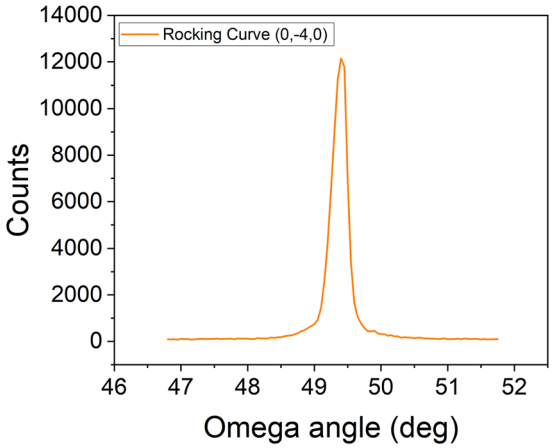

Fig. 3 Rocking curve measurement of the (0, −4, 0) reflection of $CsPbBr_3$ single crystal. In addition, the external morphology of the obtained $CsPbBr_3$ crystals was correlated with crystallographic orientation by performing face indexation based on the single-crystal XRD data. The analysis indicates that the dominant large flat faces of the cuboid correspond to the (0, 0, 1) family, while the main side facets are consistent with the (1, 1, 0) and (1, 0, 0) planes. Several smaller faces with higher-index orientations were also identified, which likely arise from slight deviations in growth conditions and local supersaturation during the final stage of crystallization. Representative face-indexation results are provided in the SI (Fig. S2). Overall, the observed well-defined low-index facets are consistent with the formation of a single-crystalline cuboid morphology.

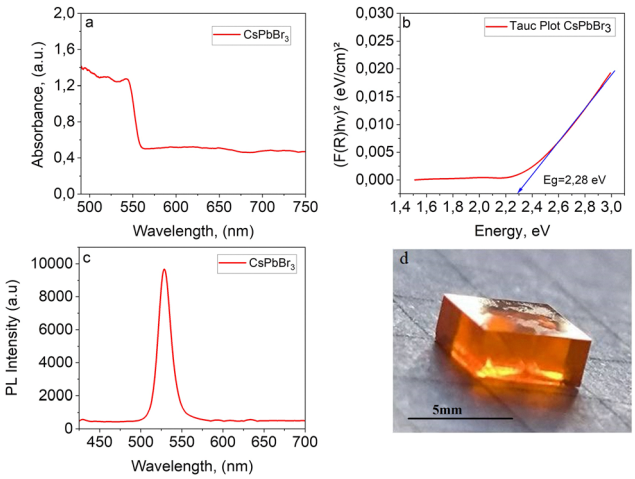

Fig. 4 (a) Optical absorption spectrum of the $CsPbBr_3$ single crystal, (b) plot of the optical bandgap calculation using the Tauc method. (c) Photoluminescence spectrum of the $CsPbBr_3$ crystal and (d) image of the perovskite single crystal grown from solution.

3.3 PL kinetics

PL decay traces as well as the IRF of the setup are presented in Fig. 5(a). Deconvolution processing allowed us to obtain reliable function of the PL decay kinetics even with such a broad IRF as shown in Fig. 5(b). Deconvolution in bi-exponential decay model (not shown here) resulted in 98% contribution of the fast component, that is visually confirmed by mostly linear dependence of the logarithm of PL intensity

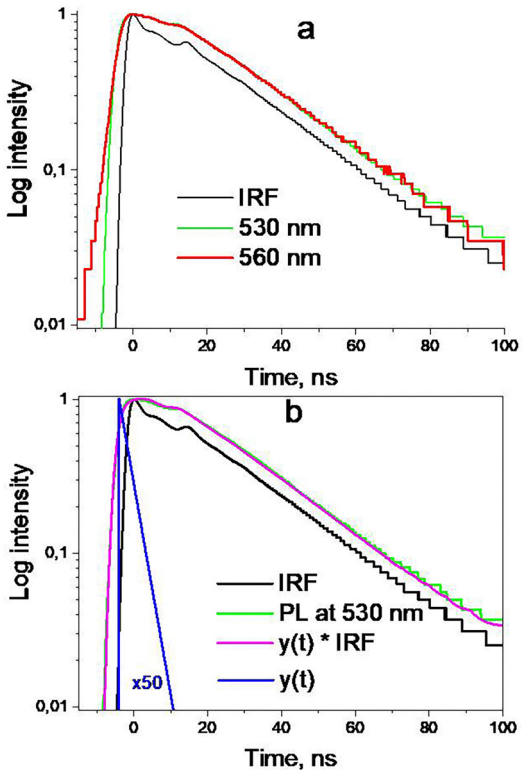

Fig. 5 (a) Experimental: IRF (black) and PL decay time traces of $CsPbBr_3$ single crystal at 530 nm (green) and 560 nm (red) detection wavelengths. (b) Processing: IRF (black), PL decay trace at 530 nm (green), mono-exponential decay function (blue) and its convolution with the IRF (magenta).

on time. Thus, the PL traces were fitted by convolution of the IRF with a sigmoidal excitation and mono-exponential decay function:

$$y(t) = a \cdot \frac{1}{1 + e^{\frac{t-\tau_0}{\tau_{ex}}}} \cdot e^{\frac{t-\tau_0}{\tau_{PL}}}$$

Here a is an intensity, τ_0 is a delay time of laser pulse (an instrumental parameter), $\tau_{ex} \ll 1$ ns is an excitation time. The PL decay time τ_{PL} is found $\sim$3 ns for both 530 nm and 560 nm PL components.

The appearance of the second emission peak is typically observed under low-temperature conditions;[24] however, it is occasionally detected even at room temperature, as reported by other authors.[23] Given that free excitons possess energies closer to the band edge, the emission band at 530 nm can be attributed to radiative recombination of free excitons. In contrast, the photoluminescence band centered at 560 nm is assigned to the emission of bound excitons, which are formed *via* interactions between excitons and defect-related or localized states.

Time-resolved photoluminescence (TRPL) analysis at 530 nm (Fig. 4a) reveals an exponential decay profile with a dominant fast component $\tau_1 \approx 3$ ns, contributing approximately 98% to the total PL intensity. This behavior is indicative of efficient radiative

recombination of free excitons and suggests minimal involvement of trap-mediated processes.

3.4 FTIR charecterization

To identify functional groups and residual surface impurities in the synthesized $CsPbBr_3$ single crystals, FTIR analysis was performed. The use of ATR-FTIR helped to eliminate background signals from the atmosphere, such as water, allowing for a more accurate interpretation of surface vibrational modes. In Fig. 6, which shows the FTIR spectrum of the synthesized perovskite single crystal, several characteristic absorption bands were detected.

The absorption band at $\sim$1075 cm^{-1} can be interpreted as the result of overlapping stretching vibrations of C–N^+ and C–O bonds in residual choline bromide, which likely adsorbed onto the crystal surface during synthesis, as mentioned by Feng *et al.*[20] Similar features were described by Cheng *et al.*[25] in their study of $CsPbBr_3$ single crystals. The peak at $\sim$1986 cm^{-1} is usually associated with vibrational modes of carbon-based residues such as C═N or C═C. However, in the context of lead based halide perovskite, especially in measurements without KBr, it is more commonly interpreted as a harmonic combination of –CH_2– bending vibrations.

The peak at $\sim$2350 cm^{-1} is well known as the carbon dioxide (CO_2) peak, which often appears during FTIR analysis conducted in non-inert conditions. It originates from ambient air and is not a characteristic feature of the $CsPbBr_3$ material itself. Similar peaks in FTIR spectra are also described in the work of Cheng *et al.*[25]

The results obtained are in good agreement with literature data for perovskite materials. In the study by Zhang *et al.*,[26] similar bands were observed in the regions of 3400 and 2920 cm^{-1} for $CsPbBr_3$ samples, which were also attributed to surface residues of organic ligands.

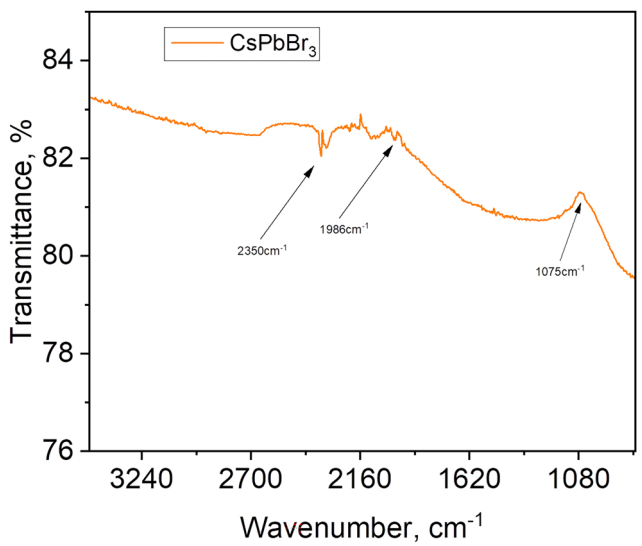

Fig. 6 FTIR spectrum of the $CsPbBr_3$ single crystal synthesized from solution.

Comparison with the literature[20,25,26] shows that the set of detected bands is consistent with data for $CsPbBr_3$ synthesized both from solution and melt. Overall, FTIR analysis confirms the integrity of the perovskite structure and the presence of residual organic components.

3.5 SEM and EDX analysis

To study the morphology of the grown $CsPbBr_3$ crystals, scanning electron microscopy (SEM) was performed at various magnification scales. In Fig. 7(a), a photo of the crystal is shown, where well-defined facets can be clearly observed. To assess the microstructure and surface defects, SEM imaging was conducted at approximately 1000× magnification at different points on the sample surface, as shown in Fig. 7(b)–(d).

Analysis of the SEM images indicates that the surface contains minor micro-defects in the form of scratches, with widths of approximately 0.1–0.3 μm (Fig. 7e).

In addition to the investigation of morphology and surface defects by scanning electron microscopy, the $CsPbBr_3$ single crystal grown from solution using the antisolvent vapor-assisted method was also analyzed by energy-dispersive X-ray spectroscopy (EDX) to evaluate its elemental composition. The EDX results confirmed the presence of cesium, lead, and bromine in ratios close to the stoichiometric composition of $CsPbBr_3$ (see Fig. S5). In addition to the main constituent elements—cesium, lead, and bromine—a small amount of carbon ($\sim$2.4%) was detected, which is likely electrically inactive and associated with residual organic species originating from the solution-based crystal growth process and/or surface handling during sample preparation. Accordingly, the EDX results are consistent with the FTIR spectroscopy data and indicate the presence of a minor amount of organic residues, predominantly confined to the near-surface regions of the crystal.

3.6 *I–V* characterization

To evaluate the charge transport semiconducting properties of $CsPbBr_3$ crystals, current–voltage (*I–V*) and photocurrent measurements were performed. A detector with an Au/$CsPbBr_3$/Au electrode configuration was fabricated from a pre-prepared $CsPbBr_3$ crystal with a thickness of 2 mm.

Fig. 8(a)–(c) shows the *I–V* characteristics measured in the dark, under ambient light, and under UV illumination at a

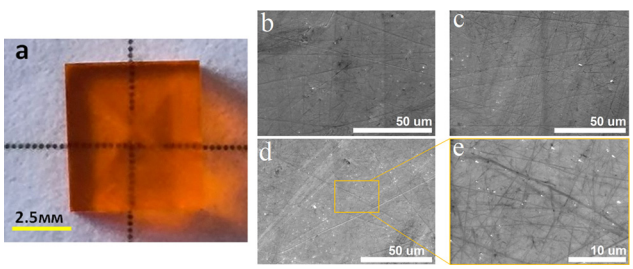

Fig. 7 Image of the $CsPbBr_3$ single crystal (a), obtained using scanning electron microscopy (SEM) at different magnifications from 1000× to 4000× (b)–(e).

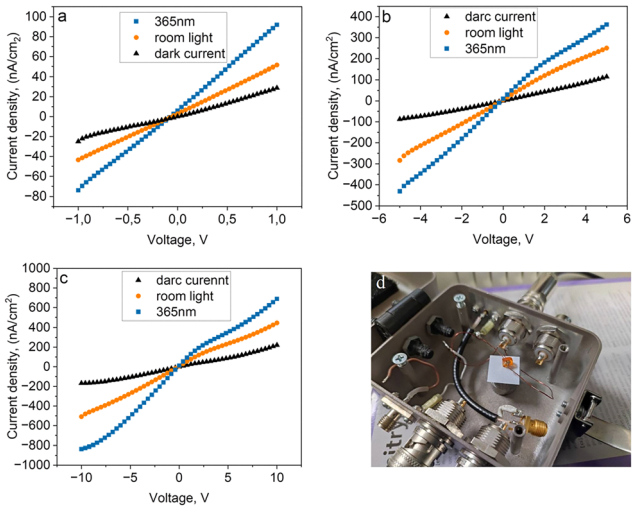

Fig. 8 (a)–(c) Current–voltage (I–V) characteristics of the $CsPbBr_3$ single-crystal-based photodetector measured under three lighting conditions: in darkness, under ambient light, and under ultraviolet illumination with a wavelength of 365 nm. The graphs show results for different voltage ranges: (a) ±1 V, (b) ±5 V, (c) ±10 V. (d) Experimental device setup for I–V, I–t measuring parameters of the $CsPbBr_3$ single crystal.

wavelength of 365 nm, for different voltage ranges (±1 V, ±5 V, ±10 V). The dark current exhibits a linear dependence on the applied voltage, indicating an ohmic contact between the electrodes and the perovskite for both bias voltage polarities. At 0 V, the dark current density was approximately 10.5 nA cm^{-2}. When exposed to ambient light, a noticeable increase in current is observed, indicating efficient photon absorption in the visible spectrum and effective photogeneration of charge carriers.

Under 365 nm (UV) illumination, a significant increase in photocurrent is observed—up to 90 nA cm^{-2} at 1 V, which is nearly 9 times higher than the dark current. This confirms high sensitivity to UV light, consistent with the bandgap of $CsPbBr_3$ (~2.2–2.4 eV).[27–29] The current curve also shows deviation from linearity at higher voltages (±10 V), which may be related to a transition to saturation or interfacial barrier effects.

These results are in good agreement with literature data for $CsPbBr_3$ single crystals synthesized *via* temperature gradient or slow evaporation methods. Zhu *et al.*[30] reported a dark current densities in the range of 10–100 nA cm^{-2} at an applied voltage of 2 V, while Huisman *et al.*[31] observed UV photocurrents in the range of 100–200 nA cm^{-2} at an applied field of 2.5 V and higher incident power densities (>1 mW cm^{-2}). In contrast, the calculated power density in this study was only ~0.2 μW cm^{-2}, resulting in an estimated responsivity of ~60 μA W^{-1} and a specific detectivity of ~1.0×10^9 Jones.

3.7 *I–t* characterization

The time-dependent photocurrent density of the $CsPbBr_3$ single crystal grown from solution was studied without an applied external voltage over a period of 600 seconds under three lighting conditions: in darkness, under ambient light, and under UV illumination.

In darkness, the current remained consistently low at around ~0.05 nA cm^{-2}. This is a critically important parameter for reducing noise and ensuring high selectivity to optical signals. Under ambient lighting, the photocurrent rapidly reached values of 2.5–4.0 nA cm^{-2} with a slight subsequent increase. Under UV illumination at a wavelength of 365 nm, an immediate increase in current density to ~6.0–7.5 nA cm^{-2} was observed, without any applied electric field. This demonstrates exceptional photoelectric sensitivity at zero bias, which is particularly important for the use of this perovskite material as a photodetector.

One of the key characteristics of photocurrent is its time response and value depending on the light source. Compared to other published works, where stable photodetector operation is achieved only under reverse bias conditions (*e.g.*, −5 V in the study by Su *et al.*[32]), in our case, the photocurrent is achieved at V = 0 V, indicating high internal efficiency of charge carrier generation and transport. For instance, J. Yu *et al.*[33] reported a current of ~2.1 nA cm^{-2} at 0 V for $CsPbBr_3$/graphene-based devices, which is lower than the values obtained in our study. Liu *et al.*[34] also noted that under 365 nm illumination and an applied voltage of 0.1 V, the photocurrent density increases to 5–10 nA cm^{-2}, which correlates well with the results obtained in our work. In the study by Chen *et al.*,[35] stable operation under 365 nm laser irradiation was achieved only with additional surface passivation, whereas our sample demonstrates a stable signal without any additional surface chemical treatment.

Thus, the presented $CsPbBr_3$ sample demonstrates competitive performance compared to previously published data. This confirms its potential for the development of low-voltage and efficient photodetectors, particularly in the UV range and beyond (Fig. 9).

To quantitatively evaluate the photoelectric response of the $CsPbBr_3$ single crystal, the spectral responsivity (R), external quantum efficiency (EQE), and specific detectivity (D^*) were calculated using the standard relations given in eqn (1)–(3). The primary photoresponse measurements were carried out under ultraviolet illumination at a wavelength of 365 nm. The photocurrent values were extracted from steady-state current–time (I–t) measurements, ensuring reliable determination of the photoresponse parameters under stabilized conditions.

$$R = \frac{I_{pc} - I_{dark}}{P_0} \quad (1)$$

$$EQE = \frac{R \cdot hc}{e\lambda} \quad (2)$$

$$D^* = \frac{R}{\sqrt{2eI_{dark}/S}} \quad (3)$$

where I_{pc} and I_{dark} are the photocurrent and dark current for the device, respectively, P_0 is the irradiation power density, S is the effective area of the detector, h is the Planck constant, c is the speed of light, λ is the wavelength of irradiation, and e is the elementary charge.

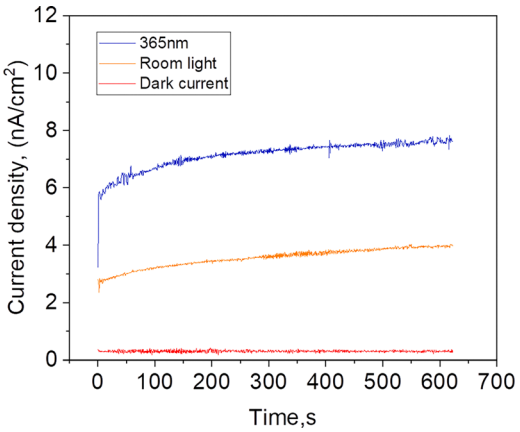

Fig. 9 Time-dependent photocurrent density of the $CsPbBr_3$ single crystal grown from solution, measured under three conditions: in darkness, under ambient light, and under ultraviolet illumination with a wavelength of 365 nm.

Additional photoresponse measurements were carried out under monochromatic visible-light illumination at a wavelength of 530 nm, using a higher illumination intensity and a small external bias voltage of +5 V. The corresponding *I–t* traces recorded in the dark and under 530 nm illumination are provided in the SI (Fig. S5). This measurement configuration was employed to obtain sufficiently high and stable photocurrent signals for reliable extraction of R, EQE, and D^*, and to enable subsequent evaluation of the charge carrier mobility–lifetime product ($\mu\tau$) using the Hecht equation. Additional experimental details of the $\mu\tau$ measurements and the Hecht-based charge collection analysis are provided in the SI.

Under 530 nm illumination, with an effective optical power of approximately 4 μW incident on the active detector area, the device exhibited a responsivity of 6.24×10^{-3} A W^{-1}, corresponding to an external quantum efficiency of approximately 1.5%, while maintaining a specific detectivity of 1.29×10^{10} Jones, enabled by the low and stable steady-state dark current. These results demonstrate that the $CsPbBr_3$ single crystal exhibits efficient photocarrier generation and a low-noise photoresponse under both ultraviolet and visible-light excitation.

The charge carrier mobility–lifetime ($\mu\tau$) product was determined by fitting the dependence of the charge collection efficiency (CCE) on the applied bias voltage using the Hecht equation. As shown in Fig. S6 the CCE increases monotonically with increasing bias and gradually approaches saturation at higher electric fields, indicating drift-dominated charge transport and progressively improved charge collection efficiency in the $CsPbBr_3$ single crystal.[9,23,36–38]

By fitting the experimental CCE–voltage characteristics, a $\mu\tau$ value of approximately 0.8×10^{-3} cm^2 V^{-1} was obtained. This value is in good agreement with previously reported data for solution-grown $CsPbBr_3$ single crystals and is comparable in order of magnitude to the $\mu\tau$ values reported for $CsPbBr_3$ single crystals grown by the Bridgman method.[8,14] This comparison indicates that the electronic transport properties of the present solution-grown crystal approach those of melt-grown counterparts.

To provide an independent assessment of the charge transport properties, the $\mu\tau$ product was also evaluated using impedance spectroscopy measurements performed under thermodynamic equilibrium (dark) conditions. From the frequency-dependent electrical modulus spectrum, the imaginary component $M''(\omega)$ exhibits a distinct relaxation peak at $f_{max} = 2.40129 \times 10^3$ Hz. According to dielectric relaxation theory, the corresponding characteristic time constant τ can be derived from:

$$\tau = \frac{1}{2\pi f_{max}} \approx 6.63 \times 10^{-5}\ \text{s}. \quad (4)$$

Assuming the relaxation process reflects the average time over which charge carriers remain mobile before recombination or trapping, and that the device geometry is a planar capacitor with inter-electrode distance $d = 2$ mm under an AC bias of 1 V, the effective drift mobility μ can be extracted *via*:[39]

$$\mu = \frac{d^2}{V \cdot \tau} \approx 6.03 \times 10^{-4}\ \text{cm}^2\ \text{V}\ \text{s}^{-1} \quad (5)$$

This yields the charge transport product:

$$\mu\tau = 4.0 \times 10^{-8}\ \text{cm}^2\ \text{V}^{-1} \quad (6)$$

The $\mu\tau$ value derived from impedance spectroscopy is significantly lower than that obtained from the Hecht analysis, reflecting the fundamental difference between equilibrium charge transport processes in the dark and the effective collection of photogenerated carriers under detector operating conditions. Accordingly, the impedance-based approach provides a reduced yet physically well-grounded estimate of the charge transport properties of $CsPbBr_3$, capturing the intrinsic equilibrium charge transport dynamics within the bulk material and complementing the photoelectrical measurements. The corresponding imaginary electrical modulus spectra used for this analysis are shown in Fig. 10.

3.8 On/off photocurrent

The photosensitivity of the $CsPbBr_3$ crystal obtained from solution was studied by measuring the photocurrent density under periodic UV light illumination (365 nm). The sample exhibited a stable and reproducible photocurrent with an amplitude of up to ~5.8 nA cm^{-2} and a low dark current level (~0.7 nA cm^{-2}), and the bulk resistivity of $CsPbBr_3$ crystal at room temperature is about 5.01×10^8 Ω cm, which is close to that of CdTe crystals.[40] These characteristics indicate high crystal quality and a low concentration of surface defects. The light response was immediate and highly repeatable. Compared to literature data for similar $CsPbBr_3$ systems,[25,41] the obtained photocurrent is competitive, considering the simplicity of the synthesis process and the absence of any need for surface modification using physico-chemical methods.

Fig. 11 illustrate the process of testing photosensitivity and the speed of charge carrier transitions between the conduction and valence bands depending on the light being turned on and off. In Fig. 11, clear periodic on/off cycles of the photocurrent

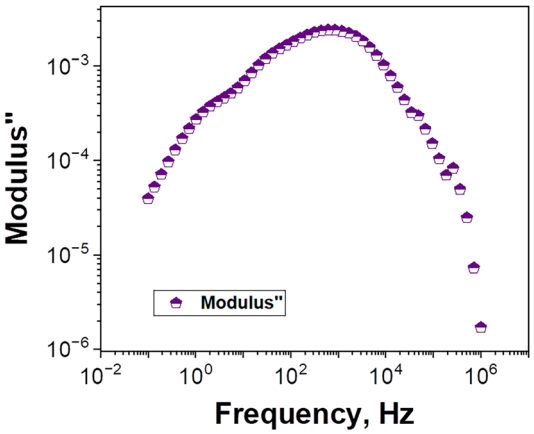

Fig. 10 Frequency dependence of the imaginary part of the electric modulus M'' for the $CsPbBr_3$ single crystal, measured *via* impedance spectroscopy under dark conditions.

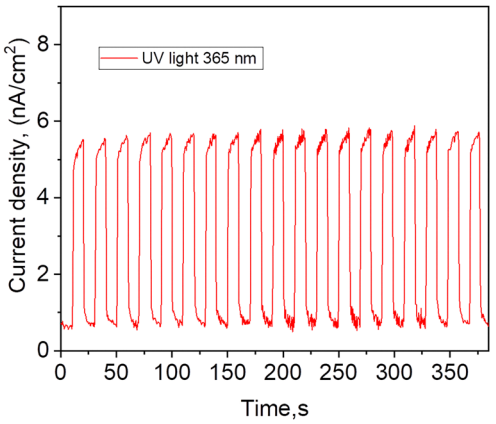

Fig. 11 Time-dependent change in photocurrent density of the $CsPbBr_3$ single crystal sample under periodic UV illumination (365 nm) during the first 400 seconds.

are visible, indicating a stable photoelectric response of the material under repeated illumination. The maximum current density reaches ~5.5–6 nA cm^{-2}, while the minimum values are close to zero, indicating a strong photoconductive switching effect.

The transitions between the "on" and "off" states have sharp edges, demonstrating a fast photoelectronic response characteristic of high-quality perovskites. The dark current (without UV) is very low (~0.5–1 nA cm^{-2}), which is a favorable property—low dark current indicates a low level of defects or surface traps. The maximum photocurrent density reached approximately 5.8 nA cm^{-2}, while under dark conditions, the current remained below 1 nA cm^{-2}, resulting in a high signal-to-noise ratio. The pulse shapes are well-defined, with immediate rise and fall times, indicating fast generation and recombination of charge carriers with no noticeable trailing effect. The current remains consistently reproducible over more than 25 illumination cycles (see SI, Fig. S3), without significant amplitude degradation.

The characteristics of the developed device are highly competitive. Published results by other authors, including Pan *et al.*,[42] reported a photocurrent of ~4.3 nA cm^{-2} for $CsPbBr_3$. Chen *et al.*[43] demonstrated a photocurrent of up to 2.4 nA cm^{-2}, but only after surface passivation with phenylethyl ammonium (PEA), whereas in our case, a pristine crystal was used without any additional chemical treatment.

Summarizing, the achieved photocurrent of our sample mainly exceeds the values of other papers based on more complex synthesis technique, showing the advantages of our simple synthesis route. This result is particularly significant considering the simplicity of the sample preparation—without passivation, physico-chemical interface treatment, or specialized electrodes.

Conclusions

In this study, $CsPbBr_3$ crystals measuring 5 × 5 × 2.6 mm were successfully grown using the AVS method. Compared to conventional growth techniques, this approach significantly enhances crystal quality, allowing the production of large, low-defect crystals without requiring highly purified precursors. Optical measurements determined a bandgap of 2.28 eV for the $CsPbBr_3$ crystals. Additionally, the rocking curve measurements allowed us to evaluate the crystallinity and purity of the $CsPbBr_3$ single crystals, confirming their high crystalline quality and good phase purity. FTIR spectroscopy indicated the presence of minor organic residues, which is consistent with previous reports. Importantly, this observation is further supported by SEM–EDX analysis, which detected a small carbon signal (~2.4%), suggesting trace surface-related organic species likely associated with the solution-based growth process and/or surface handling during sample preparation. SEM analysis of surface defects indicates minor micro-defects in the form of scratches with widths ranging from approximately 0.1 to 0.3 μm.

The obtained crystal exhibits good photosensitivity to different light sources, reaching photocurrent densities of ~2.5–4.0 nA cm^{-2} under daylight and ~6.0–7.5 nA cm^{-2} under UV irradiation (365 nm).

Furthermore, the crystals displayed a low dark current of approximately ~0.05 nA cm^{-2}, indicating a low defect density and high crystal quality. The resulting photosensitive element also shows a stable and reproducible on–off photocurrent switching behavior.

Quantitative analysis of charge transport properties revealed a mobility–lifetime product $\mu\tau$ of approximately 0.8 × 10^{-3} cm^2 V^{-1}, extracted from charge collection efficiency measurements using the Hecht equation, indicating efficient carrier transport comparable to that of $CsPbBr_3$ crystals grown by melt-based methods. Under visible-light illumination at 530 nm and an applied bias of 5 V, the devices exhibit a responsivity of 6.24 × 10^{-3} A W^{-1} and a specific detectivity of approximately 1.3 × 10^{10} Jones. Overall, these results demonstrate that the AVS-grown $CsPbBr_3$ single crystals combine favorable structural quality with competitive transport and

photoelectrical properties, highlighting their potential for application in optoelectronic devices and radiation detectors.

Conflicts of interest

There are no conflicts to declare.

Data availability

The authors confirm that data supporting the findings of this study are available within the article and its supplementary information (SI). Supplementary information is available. See DOI: https://doi.org/10.1039/d5ma01208b.

Raw data that support the findings of this study are available from the corresponding authors, upon reasonable request.

Acknowledgements

This work was partly supported by the Science@Technology Center of Ukraine under project 6437. This work was supported by a grant from the Simons Foundation (SFI-PD-Ukraine-00014579). This work was supported by MESU grants: 0124U000344, 0125U001483. VM gratefully acknowledges the financial support received from Ştefan cel Mare University of Suceava through the Technology Transfer Center in Industry 4.0 and Smart Destinations, and the Department of Electrical Engineering and Computer Science. AD acknowledges support by NASU grant no. B/290 "Femtooptics of materials for optoelectronics".

Notes and references

1 N. Gehrels, G. Chincarini, P. Giommi, K. Mason, J. Nousek, A. Wells, N. White, S. Barthelmy, D. N. Burrows and L. R. Cominsky, The Swift gamma-ray burst mission, *Astrophys. J.*, 2004, **611**, 1005.

2 J. Hugg, B. Harris and H. Tomita, *Evaluation of CZT gamma cameras for human SPECT and small FOV imaging*, Society of Nuclear Medicine, 2018.

3 K. Iniewski, CZT detector technology for medical imaging, *J. Instrum.*, 2014, **9**, C11001.

4 Q. Dong, Y. Fang, Y. Shao, P. Mulligan, J. Qiu, L. Cao and J. Huang, Electron-hole diffusion lengths >175 μm in solution-grown $CH_3NH_3PbI_3$ single crystals, *Science*, 2015, **347**, 967–970.

5 G. E. Eperon, S. D. Stranks, C. Menelaou, M. B. Johnston, L. M. Herz and H. J. Snaith, Formamidinium lead trihalide: a broadly tunable perovskite for efficient planar heterojunction solar cells, *Energy Environ. Sci.*, 2014, **7**, 982–988.

6 D. Shi, V. Adinolfi, R. Comin, M. Yuan, E. Alarousu, A. Buin, Y. Chen, S. Hoogland, A. Rothenberger and K. Katsiev, Low trap-state density and long carrier diffusion in organolead trihalide perovskite single crystals, *Science*, 2015, **347**, 519–522.

7 J. Kang and L.-W. Wang, High defect tolerance in lead halide perovskite $CsPbBr_3$, *J. Phys. Chem. Lett.*, 2017, **8**, 489–493.

8 Y. He, L. Matei, H. J. Jung, K. M. McCall, M. Chen, C. C. Stoumpos, Z. Liu, J. A. Peters, D. Y. Chung and B. W. Wessels, High spectral resolution of gamma-rays at room temperature by perovskite $CsPbBr_3$ single crystals, *Nat. Commun.*, 2018, **9**, 1609.

9 D. N. Dirin, I. Cherniukh, S. Yakunin, Y. Shynkarenko and M. V. Kovalenko, Solution-grown $CsPbBr_3$ perovskite single crystals for photon detection, *Chem. Mater.*, 2016, **28**, 8470–8474.

10 A. Kanak, O. Kopach, L. Kanak, I. Levchuk, M. Isaiev, C. J. Brabec, P. Fochuk and Y. Khalavka, Melting and crystallization features of $CsPbBr_3$ perovskite, *Cryst. Growth Des.*, 2022, **22**, 4115–4121.

11 Y. He, L. Matei, H. J. Jung, K. M. McCall, M. Chen, C. C. Stoumpos, Z. Liu, J. A. Peters, D. Y. Chung, B. W. Wessels, M. R. Wasielewski, V. P. Dravid, A. Burger and M. G. Kanatzidis, High spectral resolution of gamma-rays at room temperature by perovskite $CsPbBr_3$ single crystals, *Nat. Commun.*, 2018, **9**, 1609.

12 J. Ding, S. Du, Z. Zuo, Y. Zhao, H. Cui and X. Zhan, High detectivity and rapid response in perovskite $CsPbBr_3$ single-crystal photodetector, *J. Phys. Chem. C*, 2017, **121**, 4917–4923.

13 H. Zhang, F. Wang, Y. Lu, Q. Sun, Y. Xu, B.-B. Zhang, W. Jie and M. G. Kanatzidis, High-sensitivity X-ray detectors based on solution-grown caesium lead bromide single crystals, *J. Mater. Chem. C*, 2020, **8**, 1248–1256.

14 R. Toufanian, S. Swain, P. Becla, S. Motakef and A. Datta, Cesium lead bromide semiconductor radiation detectors: crystal growth, detector performance and polarization, *J. Mater. Chem. C*, 2022, **10**, 12708–12714.

15 M. I. Saidaminov, A. L. Abdelhady, B. Murali, E. Alarousu, V. M. Burlakov, W. Peng, I. Dursun, L. Wang, Y. He and G. Maculan, High-quality bulk hybrid perovskite single crystals within minutes by inverse temperature crystallization, *Nat. Commun.*, 2015, **6**, 7586.

16 M. I. Saidaminov, M. A. Haque, J. Almutlaq, S. Sarmah, X. H. Miao, R. Begum, A. A. Zhumekenov, I. Dursun, N. Cho and B. Murali, Inorganic lead halide perovskite single crystals: phase-selective low-temperature growth, carrier transport properties, and self-powered photodetection, *Adv. Opt. Mater.*, 2017, **5**, 1600704.

17 Y. Rakita, N. Kedem, S. Gupta, A. Sadhanala, V. Kalchenko, M. L. Böhm, M. Kulbak, R. H. Friend, D. Cahen and G. Hodes, Low-temperature solution-grown $CsPbBr_3$ single crystals and their characterization, *Cryst. Growth Des.*, 2016, **16**, 5717–5725.

18 V. Petříček, L. Palatinus, J. Plášil and M. Dušek, Jana2020 – a new version of the crystallographic computing system Jana, *Z. Kristallogr. – Cryst. Mater.*, 2023, **238**, 271–282.

19 M. Dmytruk, *Deconvolution-rs*, GitHub repository, 2023.

20 Y. Feng, L. Pan, H. Wei, Y. Liu, Z. Ni, J. Zhao, P. N. Rudd, L. R. Cao and J. Huang, Low defects density CsPbBr 3 single crystals grown by an additive assisted method for gamma-ray detection, *J. Mater. Chem. C*, 2020, **8**, 11360–11368.

21 F. Wang, H. Zhang, Q. Sun, A. B. Hafsia, Z. Chen, B. Zhang, Y. Xu and W. Jie, Low-temperature solution growth and

characterization of halogen (Cl, I)-doped $CsPbBr_3$ crystals, *Cryst. Growth Des.*, 2020, **20**, 1638–1645.

22 C. Akyel, M. Özen and S. Akbulut Özen, Facile production of $CsPbBr_3$ perovskite single-crystals in a hydrobromic solution, *Turk. J. Eng.*, 2023, **7**, 92–98.

23 H. Zhang, X. Liu, J. Dong, H. Yu, C. Zhou, B. Zhang, Y. Xu and W. Jie, Centimeter-sized inorganic lead halide perovskite $CsPbBr_3$ crystals grown by an improved solution method, *Cryst. Growth Des.*, 2017, **17**, 6426–6431.

24 C. C. Stoumpos, C. D. Malliakas, J. A. Peters, Z. Liu, M. Sebastian, J. Im, T. C. Chasapis, A. C. Wibowo, D. Y. Chung, A. J. Freeman, B. W. Wessels and M. G. Kanatzidis, Crystal Growth of the Perovskite Semiconductor $CsPbBr_3$: A New Material for High-Energy Radiation Detection, *Cryst. Growth Des.*, 2013, **13**, 2722–2727.

25 P. Cheng, Z. Liu, R. Kang, J. Zhou, X. Wang, J. Zhao and Z. Zuo, Growth and high-performance photodetectors of $CsPbBr_3$ single crystals, *ACS Omega*, 2023, **8**, 26351–26358.

26 M. Zhang, C. Huang, G. Xia, J. Liu, F. Tian, J. Zou and B. Tang, Study on the vertical Bridgman method of melt-grown $CsPbBr_3$ single crystals for nuclear radiation detection, *Struct. Sci.*, 2024, **80**, 64–71.

27 S. B. Jathar, S. R. Rondiya, B. R. Bade, M. P. Nasane, S. V. Barma, Y. A. Jadhav, A. V. Rokade, K. B. Kore, D. S. Nilegave and A. M. Funde, Facile method for synthesis of $CsPbBr_3$ perovskite at room temperature for solar cell applications, *ES Mater. Manuf.*, 2021, **12**, 72–77.

28 S. Polishchuk, M. Puppin, A. Crepaldi, G. Gatti, D. N. Dirin, O. Nazarenko, N. Colonna, N. Marzari, M. V. Kovalenko and M. Grioni, Nanoscale-resolved surface-to-bulk electron transport in $CsPbBr_3$ perovskite, *Nano Lett.*, 2022, **22**, 1067–1074.

29 H. Zhou, L. Fan, G. He, C. Yuan, Y. Wang, S. Shi, N. Sui, B. Chen, Y. Zhang and Q. Yao, Low defects, large area and high stability of all-inorganic lead halide perovskite CsPbBr 3 thin films with micron-grains *via* heat-spraying process for self-driven photodetector, *RSC Adv.*, 2018, **8**, 29089–29095.

30 L. Zhu, X. Cheng, A. Wang, Y. Shan, X. Cao and B. Cao, High performance $CsPbBr_3$ epitaxial film photodetector with ultralow dark current and record detectivity, *Appl. Phys. Lett.*, 2023, **123**(21), DOI: 10.1063/5.0176240.

31 B. A. Huisman, C. Bordoni, A. Ciavatti, M. Sessolo, B. Fraboni and H. J. Bolink, Laminated Polymer-Encapsulated Halide Perovskite Photoconductors, *Adv. Funct. Mater.*, 2024, **34**, 2308844.

32 L. Su, T. Li and Y. Zhu, A vertical $CsPbBr_3$/ZnO heterojunction for photo-sensing lights from UV to green band, *Opt. Express*, 2022, **30**, 23330–23340.

33 J. Yu, G. Liu, C. Chen, Y. Li, M. Xu, T. Wang, G. Zhao and L. Zhang, Perovskite $CsPbBr_3$ crystals: growth and applications, *J. Mater. Chem. C*, 2020, **8**, 6326–6341.

34 X. Liu, M. Xu, Y. Hao, J. Fu, F. Wang, B. Zhang, S. Bennett, P. Sellin, W. Jie and Y. Xu, Solution-Grown Formamidinium Hybrid Perovskite ($FAPbBr_3$) Single Crystals for α-Particle and γ-Ray Detection at Room Temperature, *ACS Appl. Mater. Interfaces*, 2021, **13**, 15383–15390.

35 W. Chen, L. Hu, Y. Wang, L. Huang, Z. Wang and X. Tang, Surface passivation strategies for $CsPbBr_3$ quantum dots aiming at nonradiative suppression and enhancement of electroluminescent light-emitting diodes, *Dalton Trans.*, 2025, **54**, 2156–2165.

36 X. Zhang, D. Zhao, X. Liu, R. Bai, X. Ma, M. Fu, B.-B. Zhang and G. Zha, Ferroelastic Domains Enhanced the Photoelectric Response in a $CsPbBr_3$ Single-Crystal Film Detector, *J. Phys. Chem. Lett.*, 2021, **12**, 8685–8691.

37 J. Li, X. Du, G. Niu, H. Xie, Y. Chen, Y. Yuan, Y. Gao, H. Xiao, J. Tang, A. Pan and B. Yang, Rubidium Doping to Enhance Carrier Transport in $CsPbBr_3$ Single Crystals for High-Performance X-Ray Detection, *ACS Appl. Mater. Interfaces*, 2020, **12**, 989–996.

38 J. Di, H. Li, J. Su, H. Yuan, Z. Lin, K. Zhao, J. Chang and Y. Hao, Reveal the Humidity Effect on the Phase Pure CsPbBr(3) Single Crystals Formation at Room Temperature and Its Application for Ultrahigh Sensitive X-Ray Detector, *Adv. Sci.*, 2022, **9**, e2103482.

39 J. Song, Q. Cui, J. Li, J. Xu, Y. Wang, L. Xu, J. Xue, Y. Dong, T. Tian, H. Sun and H. Zeng, Ultralarge All-Inorganic Perovskite Bulk Single Crystal for High-Performance Visible–Infrared Dual-Modal Photodetectors, *Adv. Opt. Mater.*, 2017, **5**, 1700157.

40 T. Takahashi and S. Watanabe, Recent progress in CdTe and CdZnTe detectors, *IEEE Trans. Nucl. Sci.*, 2001, **48**, 950–959.

41 H. J. Tak, J. H. Lee, S. Bae and J. W. Jo, Surface-Passivated $CsPbBr_3$ for Developing Efficient and Stable Perovskite Photovoltaics, *Crystals*, 2021, **11**, 1588.

42 L. Pan, I. R. Pandey, A. Miceli, V. V. Klepov, D. Y. Chung and M. G. Kanatzidis, Perovskite $CsPbBr_3$ Single-Crystal Detector Operating at 1010 Photons s–1 mm–2 for Ultra-High Flux X-ray Detection, *Adv. Opt. Mater.*, 2023, **11**, 2202946.

43 L. Chen, H. Wang, W. Zhang, F. Li, Z. Wang, X. Wang, Y. Shao and J. Shao, Surface Passivation of $MAPbBr_3$ Perovskite Single Crystals to Suppress Ion Migration and Enhance Photoelectronic Performance, *ACS Appl. Mater. Interfaces*, 2022, **14**, 10917–10926.